High-Entropy Driven Half-Heusler Alloys Boost Thermoelectric Performance

Subrata Ghosh[1]*, Amin Nozariasbmarz[1], Huiju Lee[2], Lavanya Raman[1], Shweta Sharma[1], Rabeya B. Smriti[1], Dipika Mandal[3], Yu Zhang[1], Sumanta K. Karan[1], Na Liu[1], Jennifer L. Gray[4], Mohan Sanghadasa[5], Yi Xia[2]*, Shashank Priya[1], Wenjie Li[1]*, and Bed Poudel[1]*

[1]Department of Materials Science and Engineering, Pennsylvania State University, University Park, PA 16802, United States

[2]Department of Mechanical and Materials Engineering, Portland State University, Portland, OR 97201, United States

[3]Department of Mechanical Engineering and Materials Science, University of Pittsburgh, Pittsburgh, PA 15260, United States

[4]Materials Research Institute, Pennsylvania State University, University Park, PA 16802, United States

[5]U.S. Army Combat Capabilities Development Command Aviation & Missile Center, Redstone Arsenal, AL, 35898, USA

*Email: smg7204@psu.edu (S.G.), yxia@pdx.edu (Y.X.), wzl175@psu.edu (W.L.), and bup346@psu.edu (B.P.)

SUMMARY

High-entropy engineering effectively reduces lattice thermal conductivity (κ_L) in thermoelectric (TE) materials; however, the chemical complexity of multiple elements in high-entropy materials often leads to phase segregation, limiting their electrical transport properties and overall, TE performance. Herein, we reported a *p*-type high entropy stabilized single-phase half-Heusler alloy, *M*FeSb, specifically designed to enhance configurational entropy by introducing multiple element species on a single atomic site. This material exhibited low κ_L due to strong phonon scattering and phonon group velocity reduction from lattice strain generated through distorted lattices while maintaining a high power-factor. The material demonstrated a record high figure-of-merit (zT) of 1.5 at 1060 K, with an average zT of ~0.92 over 300-1060 K. Furthermore, superior conversion efficiency of 15% and 14% for a single-leg and a unicouple module at a temperature difference of $\Delta T \sim 671$ K were achieved. Our findings provide a new avenue for enhancing TE materials performance through high-entropy engineering.

KEYWORDS

High entropy engineering; Thermoelectric effect; half-Heusler; figure of merit; Thermoelectric conversion efficiency; hardness

INTRODUCTION

Thermoelectric generators (TEGs) offer an eco-friendly energy conversion technology to directly convert heat into electricity through the Seebeck effect, promoting the efficiency of fuel utilization and sustainable energy development.[1–5] To enhance the feasibility of TEGs, it is essential to improve the energy conversion efficiency (η) which primarily depends on the dimensionless figure of merit, $zT = S^2\sigma T/\kappa$ where S is the Seebeck coefficient, σ, is the electrical conductivity, T, is the absolute temperature, and κ, is the total thermal conductivity, comprising of the electronic thermal conductivity (κ_{el}) and lattice thermal conductivity (κ_L). η of a TEG demands a high average zT, (zT_{avg}), over a wide range of operating temperatures. To achieve high TE properties, the materials with a high power-factor ($PF = S^2\sigma$) and/or low κ are required.[6–12] However, these TE parameters (κ, σ and S) are strongly correlated to each other and influenced by the carrier concentration (n_H) and carrier mobility (μ_H). Generally, two principal strategies have been employed to enhance the performance of TE materials:[3] modifying electronic band structure to increase the density of states' effective mass that contributes to high PF,[13–15] and introducing extrinsic defects through nanostructuring to enhance phonon scattering that reduces κ_L.[2,16]

Entropy engineering has recently become a compelling strategy for synergistically optimizing the electrical and thermal properties of various TE materials, particularly the design of high-entropy alloys (HEAs).[8,9,17,18] Typically composed of five or more principal elements, HEAs exhibit a substantial configurational entropy ($\Delta S_{conf} > 1.5\ R$, where R is gas constant).[19] The introduction of a greater number of element species enhances S_{conf}, leading to the stabilization of the crystal phase at elevated temperatures by reducing the Gibbs free energy. Consequently, entropy-engineered single-phase stabilization mitigates phase boundary scattering of electrons, preserving the electrical transport properties in HEAs.[9] Meanwhile, due to the chemical complexity of the material (such as atomic size and mass mismatches), severe lattice distortion is generated in a short-range order which enhances the scattering of the heat carrying phonons that in turn reduces κ_L significantly.[20] Additionally, the high-entropy effect decreases the grain sizes, further contributing to κ_L reduction and potentially enhancing mechanical strength.[19] So far, entropy engineering has successfully enhanced zT in TE materials such as PbSe[9,17] and GeTe[8] based chalcogenides by tuning electron and phonon transport.

Half-Heusler (hH) materials have garnered significant attention for medium to high-temperature TE applications due to the combination of their exceptional electrical properties, excellent thermal stability, and robust mechanical strength.[10,14,21–26] The current state-of-the-art hH materials exhibit a relatively low zT compared to other classes of materials, primarily due to their high κ. Several approaches have been emerged to enhance TE performance of hH materials including nanostructuring,[25] defects chemistry,[23] band engineering,[24] and resonant dopant.[27] The entropy engineering has also been explored in hH systems but their zT performance is rather poor compared to chalcogenide-based TE materials.[28] In this study, we successfully designed a high-entropy p-type MFeSb-based hH alloy by introducing multiple elements (Nb, Ta, Ti, V with an equimolar ratio) on a single atomic site (M: 0,0,0-Wykoff site of the hH phase). This approach is proved to be an effective strategy to develop high-entropy hH TE materials to optimize κ_L and PF simultaneously (**Figure 1A**). The resulting high-entropy MFeSb hH alloy exhibits low κ_L of 2 W m^{-1} K^{-1} at room temperature while maintains a high PF of ~37.3 μW cm^{-1} K^{-1}. Consequently, it exhibits a superior peak zT of 1.5 at 1060 K (**Figure 1B**) and an zT_{avg} of 0.92 between 300 –1060

K (**Figure 1C**), which is surpassing the state-of-the-art TE materials in medium to high-temperature.[23–25,28–30] These exceptional TE properties are further validated experimentally by fabricating single-stage modules, with η reaching 15% for a single-leg and ~14% for a unicouple module at ΔT = 670 K, which are the highest η among the state-of-the-art results including both single-stage and segmented TE modules (**Figure 1D**).[8,9,38–41,17,31–37]

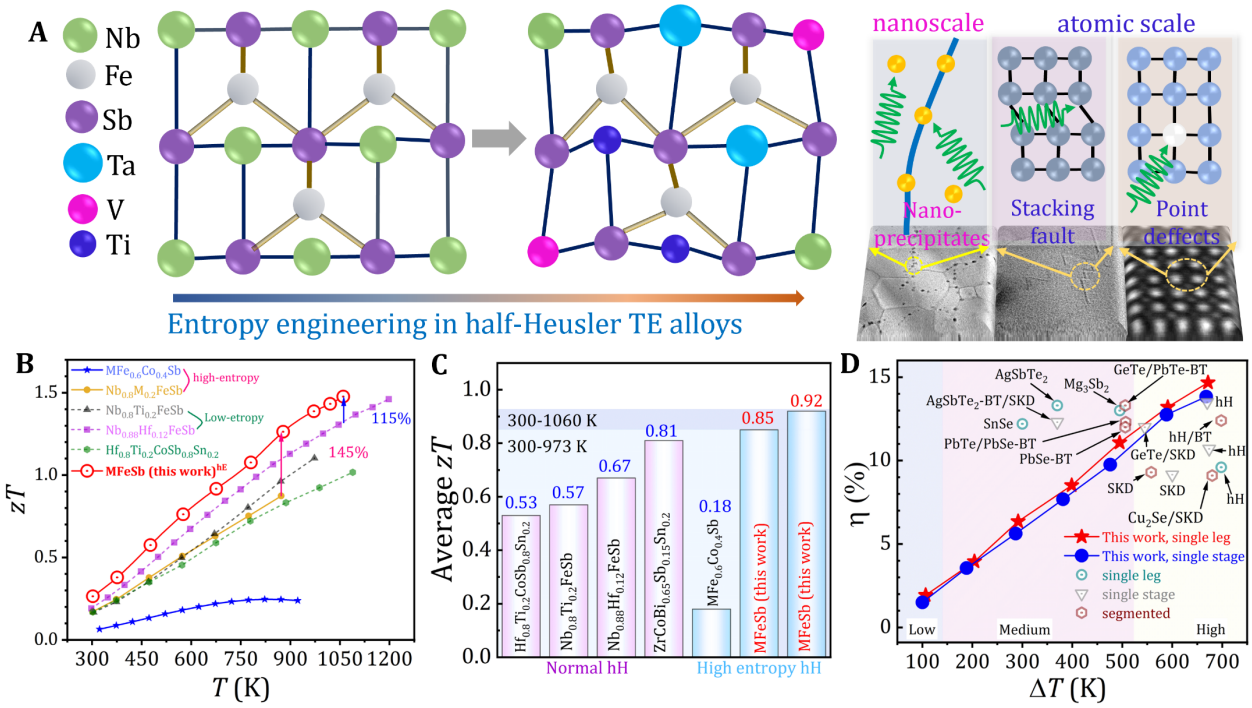

Figure 1. High entropy engineering and TE performance of MFeSb hH alloy.

(A) Schematic diagram of entropy engineering effect in MFeSb-based hH alloys (left) and corresponding multiple phonon scattering sources in different length scales (Right).
(B and C) Temperature-dependent (B) peak zT and (C) zT_{avg} among high-entropy engineered MFeSb hH alloys developed in this study and state-of-the-art TE hH materials.[23–25,28–30] (zT value show significant improvement about 145% of the best value reported in high-entropy engineered hH and 115% of low-entropy NbFeSb based hH).
(D) Maximum η as a function ΔT for the high entropy engineered MFeSb-based single leg and unicouple module. For comparison, some reported state-of-the-art module results are included.[8,9,38–41,17,31–37]

RESULTS AND DISCUSSION

The single-phase stabilized hH phase ($F\bar{4}3m$ cubic structure) is observed for high-entropy $Nb_{0.25}Ta_{0.25}Ti_{0.25}V_{0.25}FeSb$ sample at various sintering temperatures (**Figure 2A**). The calculated lattice parameter by Rietveld refinement is 0.5923 nm (**Figure S1**). Microstructural analysis using high-angle annular dark field (HAADF) and energy dispersive spectroscopy (EDS) via scanning transmission electron microscopy (STEM) reveals nanoprecipitates, primarily Ti-riched, concentrated along grain boundaries and sporadically within grains (**Figure 2B–2I**, and **Figure S2** to **S6**). These nanoprecipitates have a diameter less than 10 nm which often led to stacking faults in the matrix (**Figure 2F** and **Figure S7**).[17] High-resolution STEM-HAADF images along the [100] zone axis with intensity scan profiles confirms the periodicity of the atomic arrangement of

the constituting elements which indicates the crystallinity of the high-entropy composition (**Figure 2G–2H**). The unambiguous intensity contrast indicated in the line scan illustrates atomic vacancies of Fe-site (**Figure 2H**) which are often generated through alloying effects due to mass and strain field fluctuation between the alloying atoms.[23,42] The single phase of the MFeSb matrix was further confirmed by indexing diffraction spots in the selected area electron diffraction (SAED) patterns of the HRTEM image (**Figure 2I** and **Figure S8**). The high-entropy effect results in a substantially reduced grain size with an average grain size of ~100 nm (**Figure S9**) which is significantly smaller compared to the low-entropy NbFeSb hH alloy (~ 700 nm), prepared by a similar method (**Figure S10**).

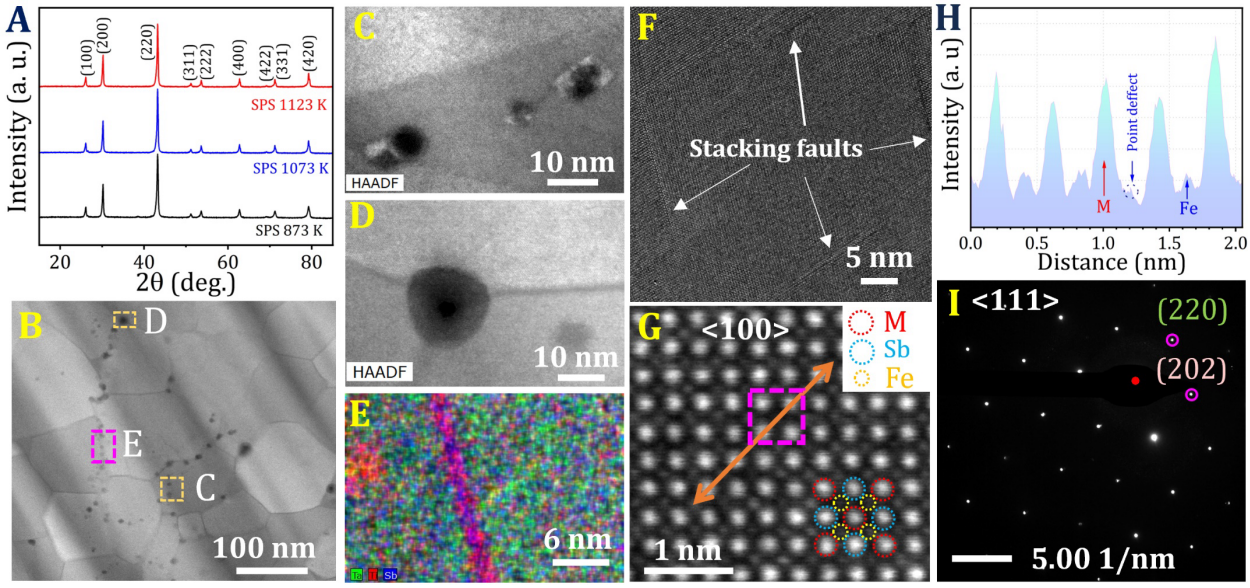

Figure 2. Stabilization of single-phase structure and generation of defects due to high entropy effect.
(A) XRD patterns of MFeSb alloy prepared under different SPS temperatures.
(B) STEM image demonstrates the grains with nanoprecipitates.
(C–F) HAADF images of nanoprecipitates (C) within the grains, (D) at the triple point of grain boundaries, and (E) EDS mapping across the grain boundaries demonstrates the Ti-rich nanoprecipitates.
(F) Stacking faults in the phase matrix.
(G and H) (G) High resolution STEM HAADF images showing the ordered crystal structure and (H) the intensity scan profile of the indicated arrow in (G) exhibits the existence of point defect, shown by blue circle.
(I) The [111] zone-axis selected area electron diffraction pattern demonstrates the crystallinity of phase.

Lattice distortions in short-range order due to chemical complexity at M-site, induced by the high-entropy effect, can significantly impact the electrical and thermal transport properties of hH alloys.[8,9] MFeSb exhibits characteristics of a heavily doped *p*-type semiconductor with sustained high hole concentration (n_H ~5×10^{20} cm^{-3}) which remain almost independent of temperature (**Figure S11**). The mitigation of electron scattering near the phase boundary preserves high μ_H of 20.6 cm^2 V^{-1} s^{-1} at room temperature, indicating the electronic transport is merely hampered due to the single-phase formation driven by high-entropy effect. The electrical conductivity is slightly low compared to low-entropy NbFeSb-based hH alloys[23,29,43] due to suppressed n_H and shows a

metal-like behavior (**Figure 3A**). The temperature dependency of σ reveals the dominating carrier scattering mechanism; acoustic phonon scattering prevails when σ follows a $T^{-1.5}$ behavior while disorder or alloy scattering is prevalent with $\sim T^{-0.5}$ dependence.[44] Acoustic phonon scattering is predominant to charge transport in most of the low-entropy TE materials.[23,29] In high-entropy MFeSb, σ roughly follows $T^{-0.6}$ behavior, suggesting the disorder or alloys scattering generated from the high-entropy effect dominates the electrical transport rather than acoustic phonon scattering. The large S remains preserved due to the single-phase formation of the sample, and it approaches ~215 μV K^{-1} at higher temperatures (**Figure 3B**). Consequently, a high average PF of 33.6 μW cm^{-1} K^{-1} over the temperature regime of 300-1060 K was maintained (**Figure 3C**). The maximum PF of 37.3 μW cm^{-1} K^{-1} is obtained at 973 K, a significantly high value compared to the reported high entropy engineered TE materials (**Figure S12**).

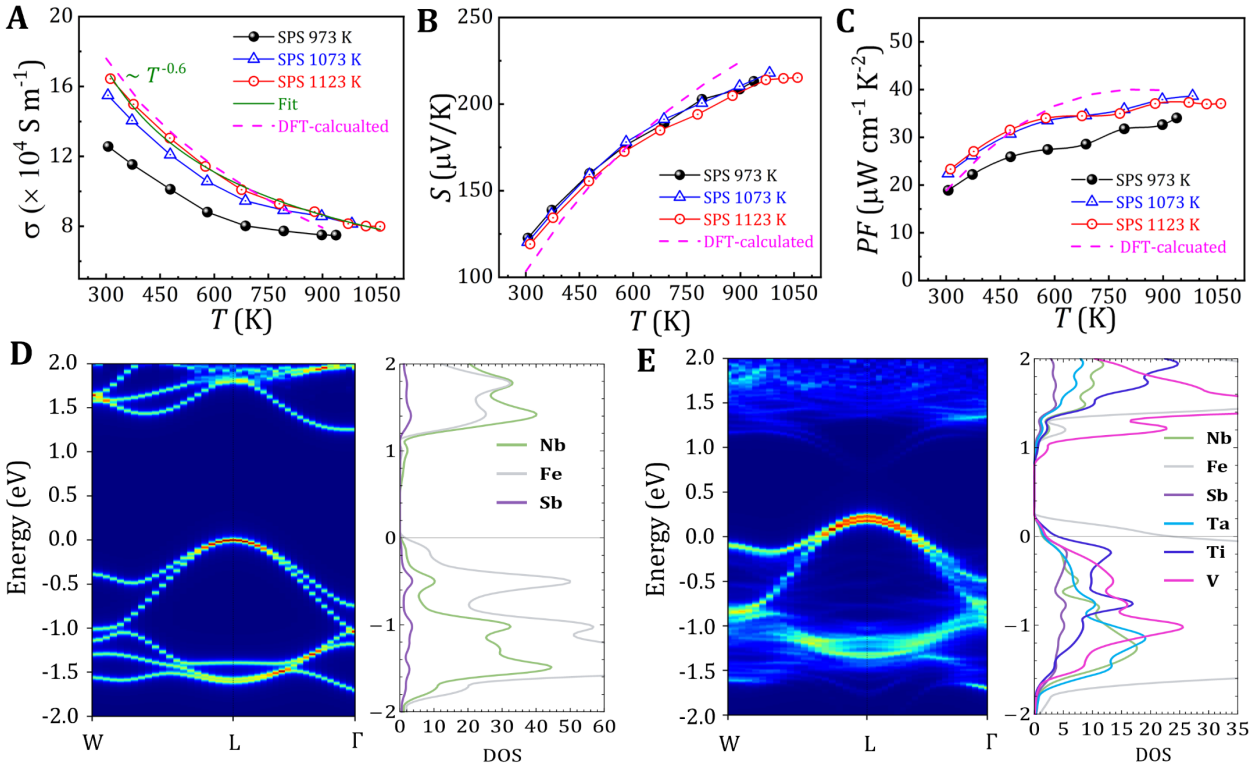

Figure 3. Electrical transport properties of high entropy MFeSb alloy.
(A–C) Temperature dependence of experimental (A) σ, (B) S, and (C) PF of MFeSb sintered at 1123 K with DFT calculated electrical properties.
(D and E) Calculated electronic band structure (left panel) and the corresponding atom-decomposed density of states (DOS) (right panel) of (D) NbFeSb and (E) MFeSb.

To understand the impact of the high-entropy effect on electronic transport properties, we conducted first-principles calculations of band structures and density of states (DOS) using density functional theory (DFT) for stoichiometric NbFeSb and high-entropy MFeSb hH compounds. The calculated band structure reveals the valence band maximum at the L point with two-fold degeneracy (**Figure 3D**), which is consistent with prior literature.[45] This is particularly significant

as hole carriers predominate in our synthesized samples. The corresponding DOS indicates that the high-lying valance bands are dominated by Fe atoms, followed by Nb and Sb atoms. Therefore, it is expected that the key features associated with the valence band maximum persist in high entropy MFeSb. To incorporate the configurational order in MFeSb, we constructed a supercell with 16 formula units of NbFeSb and then populated the Nb sites with an equal molar ratio of M elements using the special quasirandom structures (SQS) approach.[46] The band structure and DOS were visualized using the electronic band unfolding approach (**Figure 3E**) (folded band structure in **Figure S13**).[47] Notably, the high-lying valence bands display a similar shape to **Figure 3D** due to the dominance of Fe characters. However, MFeSb exhibits several distinctions. First, slight band splitting of the top valence bands occurs due to the symmetry breaking induced by disorder, potentially suppressing the carrier transport. Second, the unfolded electronic band structure of MFeSb exhibits considerable broadening due to the presence of disorder, which is in line with the experimental observation where alloying scattering dominates the total carrier scattering. Third, the Fermi level shifts into the high-lying valence band compared to NbFeSb, a consequence of electrons deficiency from M alloying elements. A detailed electron count indicates the introduction of an equal molar ratio of M elements results in 0.25 holes per formula unit, explaining the intrinsic heavy hole doping in our synthesized samples. It is worth noting that due to the presence of various kinds of defects (e.g., precipitates), the measured hole concentrations in experimentally synthesized samples might deviate from our theoretical calculations. Using the band structure in **Figure 3E**, we computed the electrical transport properties (**Figure 3A–3C**). By gauging a hole concentration that can faithfully reproduce the temperature dependent S and fitting a temperature-dependent carrier lifetime (**details are in supplemental information (SI)**), we achieve semiquantitative agreement with experimental data on σ and PF. Overall, our results show that the primary features of the electronic band structure of NbFeSb persist in MFeSb, elucidating the achieved high PF in high entropy hH while also emphasizing the impact of disorder/alloying scattering introduced by M alloying elements.

While preserving high electrical transport properties, the high-entropy effect suppresses κ of MFeSb significantly as well. The temperature dependence of κ is presented in **Figure 4A**. The κ_L is obtained by subtracting κ_{el} based on the Wiedmann-Franz law from κ (**details are in SI, Figure S14** and **Table S1**). The κ initially decreases with increasing temperature, then increases after ~780 K due to an increase in the electronic component of κ (**Figure S14E**). High-entropy engineering results into a substantially reduced κ_L ~2 W m^{-1} K^{-1} at room temperature, around nine times lower than the low-entropy pristine NbFeSb alloy (~17 W m^{-1} K^{-1})[29] (**Figure 4B**). This low κ_L persists throughout the temperature range, approaching 1.67 W m^{-1} K^{-1} at 900 K (**Figure S14F**). Such a remarkable reduction in κ_L is often attributed to the enhanced phonon scattering induced by severe lattice strain from the distorted lattice,[8,9,17] which is associated with the increased S_{conf} in MFeSb due to significant changes in atomic masses and sizes of the M-site elements. A monotonic reduction in κ_L of NbFeSb-based hH alloys with increased entropy was demonstrated in **Figure 4B**. The fundamental source of high-frequency phonon scattering in the HEAs is severe lattice distortion.[9] Moreover, the phonons with higher frequencies are scattered by the point defects. The observed nano-precipitates near the grain boundary, and stacking faults contribute to acoustic phonons scattering. The small average sizes of the high-density nano-precipitates around 10 nm primarily induce low-frequency phonon scattering,[17] while the stacking faults on a scale below 10 nm are responsible for the mid-frequency phonon scattering. The reduced average grain size of high entropy MFeSb (~100 nm) further triggers grain boundary

scattering, playing a pivotal role in diminishing κ_L. Furthermore, the presence of riched Ti element causes deceleration of optical phonon while the apparent reduction of group velocity in acoustic phonon might be introduced by heavy element, Ta[48]. Additionally, we observed the reduction of low sound velocity (v) in high-entropy MFeSb (~ 2820 ms^{-1}) compared to pristine NbFeSb (~ 3388 ms^{-1}) (**Figure S15**), further reducing κ_L.

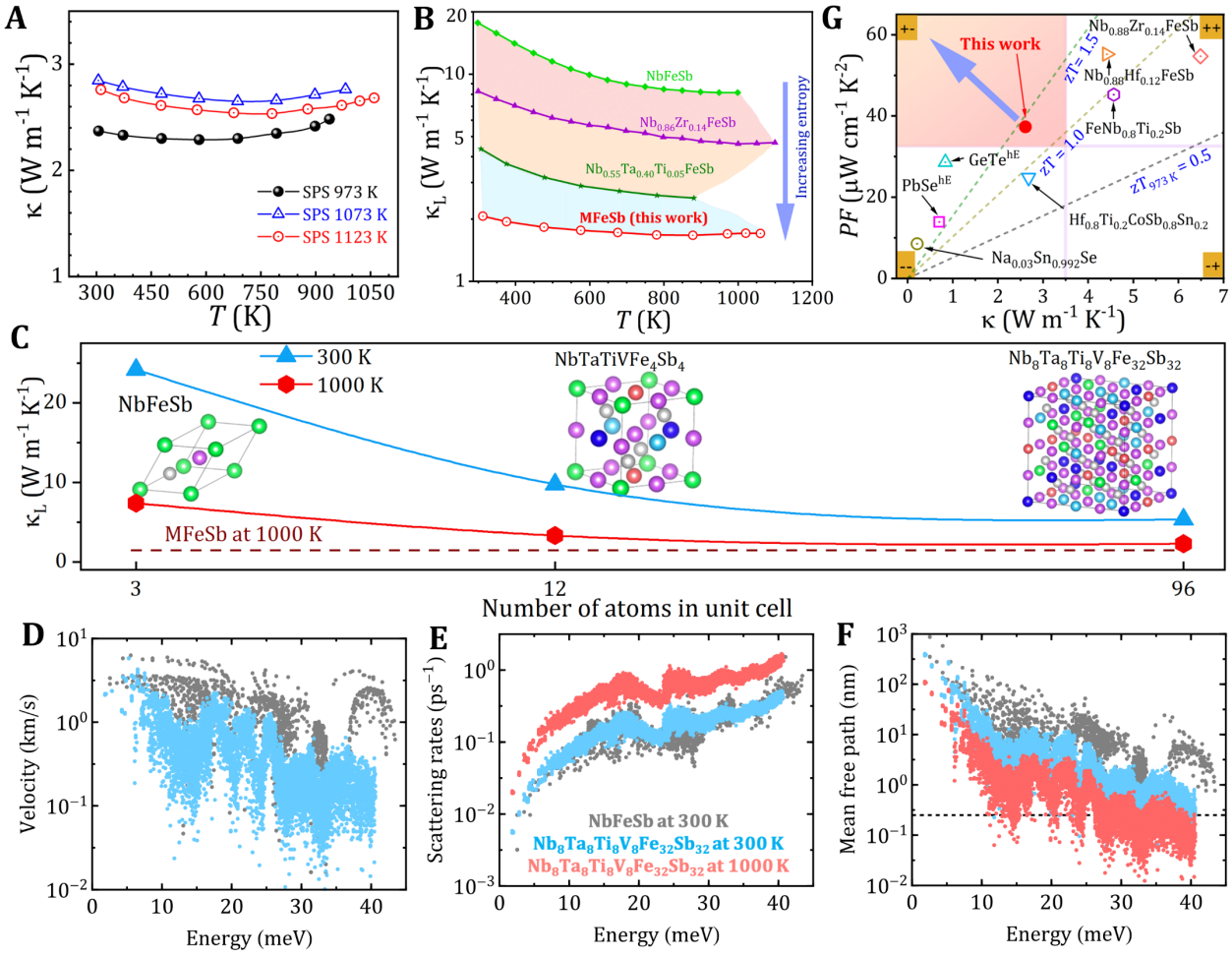

Figure 4. Thermal transport properties and first-principles simulation of κ_L.
(A) Total thermal conductivity of MFeSb alloy prepared under different sintered temperatures.
(B) Entropy increasing effect to the reduction in κ_L of hH phase. To demonstrate the effect, we have included the data of NbFeSb,[29] $Nb_{0.86}Zr_{0.14}FeSb$,[23] $Nb_{0.55}Ta_{0.40}Ti_{0.05}FeSb$.[21]
(C–F) (C) Calculated κ_L for NbFeSb and MFeSb at 300 K and 1000 K. The disorder on M sites is simulated using supercells containing 4 and 32 formula units (denoted as $NbTaTiVFe_4Sb_4$ and $Nb_8Ta_8Ti_8V_8Fe_{32}Sb_{32}$, respectively), as shown by the insets that depict the crystal structures. Comparison of (D) phonon mode-resolved group velocities, (E) phonon mode-resolved scattering rates, and (F) phonon mode-resolved mean free paths of NbFeSb at 300 K (gray dots), and $Nb_8Ta_8Ti_8V_8Fe_{32}Sb_{32}$ at 300 K (blue dots) and 1000 K (red dots), respectively.
(G) PF as a function of κ for various state-of-the-art results TE materials at 973 K [7–9,14,23,25]. The "+-", "++", "--" and "-+" represent high PF-low κ, high PF-high κ, low PF-low κ, low PF-high κ. For practical application, the shaded region (+-) is desired and surely, the positive effect of high entropy approach to

optimize TE properties of hH phases. The dashed lines indicate different zT values at 973 K. The PF and κ of medium temperatures TE materials such as GeTe,[8] PbSe,[9] and SnSe[7] included in the graph are collected at 873 K.

To unravel the intrinsic effects of high-entropy on lattice heat transfer in MFeSb, particularly in the absence of various defects, we conducted explicit calculations of κ_L in both NbFeSb and MFeSb. We adopted finite-size supercell structures to model the disorder in MFeSb. Two supercells containing 4 and 32 formula units were generated and then populated with an equal molar ratio of M elements on the Nb sites using SQS approach.[46] The resulting compounds are denoted as $NbTaTiVFe_4Sb_4$ and $Nb_8Ta_8Ti_8V_8Fe_{32}Sb_{32}$, respectively (inset of **Figure 4C**). Using these supercells, we calculated κ_L using a theoretical framework that combines anharmonic lattice dynamics[49] and the unified thermal transport theory.[45] To minimize the substantial computational expense associated with calculating anharmonic force constants directly from the first principles, we trained a moment tensor machine learning potential[50,51] for disordered MFeSb (**details can be found in SI**). We find that κ_L at 300 K is significantly reduced from 24.7 W m^{-1} K^{-1} in NbFeSb to 10.3 W m^{-1} K^{-1} in $NbTaTiVFe_4Sb_4$, and further to 5.7 W m^{-1} K^{-1} in $Nb_8Ta_8Ti_8V_8Fe_{32}Sb_{32}$ (**Figure 4C**). These results unambiguously demonstrate that high-entropy effect can significantly reduce κ_L. When the temperature is increased to 1000 K, κ_L of $Nb_8Ta_8Ti_8V_8Fe_{32}Sb_{32}$ further decreases to 2.3 W m^{-1} K^{-1}, which is approaching the experimental value of 1.7 W m^{-1} K^{-1} of MFeSb at 1000 K. We note that our calculated κ_L is still higher than the experiments, which is likely due to the adopted finite sizes of disordered supercells. In addition, our theoretical calculations do not account for phonon scatterings beyond intrinsic phonon-phonon interactions, such as those due to electron-phonon interactions, nano-precipitates, and grain boundaries. To reveal the microscopic mechanism responsible for the reduction of κ_L, we present the comparison of phonon group velocities, scattering rates, and mean free paths between NbFeSb and $Nb_8Nb_8Ta_8Ti_8V_8Fe_{32}Sb_{32}$ (**Figure 4D–4F**). We observe that the high-entropy effect drastically reduces the phonon group velocities (**Figure 4D**). This reduction is attributed to the folding and flattening of phonon dispersion caused by the complex structure of MFeSb (**Figure S16**, **Figure S17A** and **S17B**). Somewhat unexpectedly, the comparison of phonon scattering rates between NbFeSb and $Nb_8Ta_8Ti_8V_8Fe_{32}Sb_{32}$ at 300 K shows that phonon scattering rates seem to be less affected by the disorder (**Figure 4E**), especially compared with the group velocities. The combined alloying effects on phonon group velocities and scattering rates are reflected in the phonon mode-resolved mean free path (**Figure 4F**). We observe that optical phonons with higher energy levels experience significant scattering, resulting in shorter mean free paths. In contrast, the lower-energy acoustic modes maintain relatively longer mean free paths, amenable to scattering interactions with defects present in the synthesized samples, including point defects, grain boundaries, precipitates, and stacking faults. For instance, examining the cumulative κ_L as a function of the mean free path in MFeSb (**Figure S18**), it is evident that grain sizes with dimensions of 10 nm can substantially decrease κ_L to below 2.0 W m^{-1} K^{-1}.

To gain deeper insights into the reduction of group velocities, we calculated the phonon participation ratio (**Figure S17E** and **S17F**), a quantity that measures the degree of spatial localization of a vibrational mode.[52–54] The phonon participation ratio is defined as the fraction of atoms participating in a given vibrational mode, with a value close to one indicating a delocalized mode and a value approaching 1/N (where N is the number of atoms in the system) indicating a highly localized mode. Our analysis reveals that the phonon participation ratios of most phonon

modes in MFeSb are significantly lower than those in NbFeSb, providing clear evidence of strong phonon localization in MFeSb. This localization arises from the disorder-induced breaking of translational symmetry, which leads to the confinement of vibrational modes to smaller regions of the lattice. Consequently, the localized modes have reduced group velocities, as they are less effective at propagating heat through the lattice. It is worth noting that our measured reduction in sound velocity aligns with our calculations, albeit with a less pronounced reduction. This is because the measured sound velocity primarily captures the behavior of long-wavelength acoustic phonon modes and does not account for the contributions of optical modes, which are more strongly affected by localization. In summary, our explicit calculations provide strong evidence that the intrinsic high-entropy effect plays a more crucial role in directly reducing phonon group velocities through localization than in affecting phonon scattering rates. This localization mechanism ultimately leads to a substantial decrease in the κ_L of MFeSb compared to NbFeSb.

The synergistically optimized high PF and reduced κ results in a remarkably high zT of ~1.5 at 1060 K in MFeSb alloy (**Figure 1B** and **Figure S19**). The zT_{avg} is the utmost parameter towards high η. The zT_{avg} is 0.85 and 0.92 within temperature regime of 300-973 K and 300-1060 K, respectively, which is superior compared to conventional and other high-entropy p-type hH materials reported so far (**Figure 1C**). MFeSb also demonstrates excellent repeatability of TE performance, validated through three different batches of samples (**Figure S20).** For all types of TE materials, it is crucial and challenging to decouple TE parameters to achieve high PF and low κ simultaneously. Most state-of-the-art TE materials excel in either power factor or thermal conductivity[7–9,14,23,25]. Conventional hH materials usually introduce "dual-high" (PF and κ) features ("++" region in **Figure 4G**), which limit the further enhancement of TE performance. While the high entropy design in MFeSb uniquely showcases the possibility in achieving high PF and low κ simultaneously ("+-" region in **Figure 4G)**, towards further breakthrough of zT.

The remarkable TE performance is further validated by measuring the η and the output leg power density (ω_{out}). The experimental details on module fabrication and testing can be found in the **SI**. **Figure 5A** and **5B** show the ω_{out} and η of the single-leg as a function of applied current (I) under different ($\Delta T = T_h - T_c$, where T_h and T_c are the hot and cold side temperatures of the TE device). Single-leg demonstrates a superior high η of 15% at ΔT of 671 K (T_c ~ 300-320 K), which is the highest η among the reported high-performance TE modules (**Figure 1D**). A ω_{out} of ~ 3.9 W cm^{-2} is achieved at the same ΔT. Furthermore, we fabricated a unicouple TE module using high entropy p-type MFeSb and an n-type ZrNiSn-based material[55] (details of fabrication and TE properties of n-type material can be found in **SI**). We considered a good match of thermal expansion coefficients to choose the suitable n-type material (**Table S2**). The unicouple module exhibits a ω_{out} of ~5.3 W cm^{-2} (**Figure 5C**) and a superior η of ~14 % (**Figure 5D**) at ΔT of 670 K (T_c ~ 300-336 K), which is the highest η among all π-type TE modules (**Figure 1D**). The measured parameters of single-leg and unicouple module, such as open-circuit voltage (V_{oc}), device voltage (V_d), internal resistance (R_i) and the heat flux (Q) as a function of ΔT are shown in **Figure S21**. All the experimental results align well with theoretical calculations (**Figure 5E**, and **Figure S22**). We have carried out the measurement under a high vacuum (~10^{-7} mbar) to reduce the heat conduction and to maximize the measured η, we have chosen the coordinated geometric configuration of n- and p-type legs based on their thermal transport properties.[56] The single-leg and unicouple module exhibit excellent repeatability under multiple measurements and across three different fabricated modules (**Figure 5E, Figure S23** and **S24**).

In addition to favorable TE properties and matching thermal expansion coefficients between p-type and n-type legs, outstanding mechanical properties of TE materials play a pivotal role in durable and long-term device performance, often governed by Vickers hardness and fracture toughness.[3] High entropy engineering has been effectively utilized in refractory alloy design to improve mechanical properties.[57,58] An exceptionally high Vickers hardness of ~10.27 GPa is achieved in high entropy MFeSb, which is larger than that of conventional hH materials and significantly higher than other TE materials (**Figure 5F**).[3,22,59,60] The reduction in grain sizes due to the high-entropy effect is primarily responsible for the significant improvement of mechanical properties.

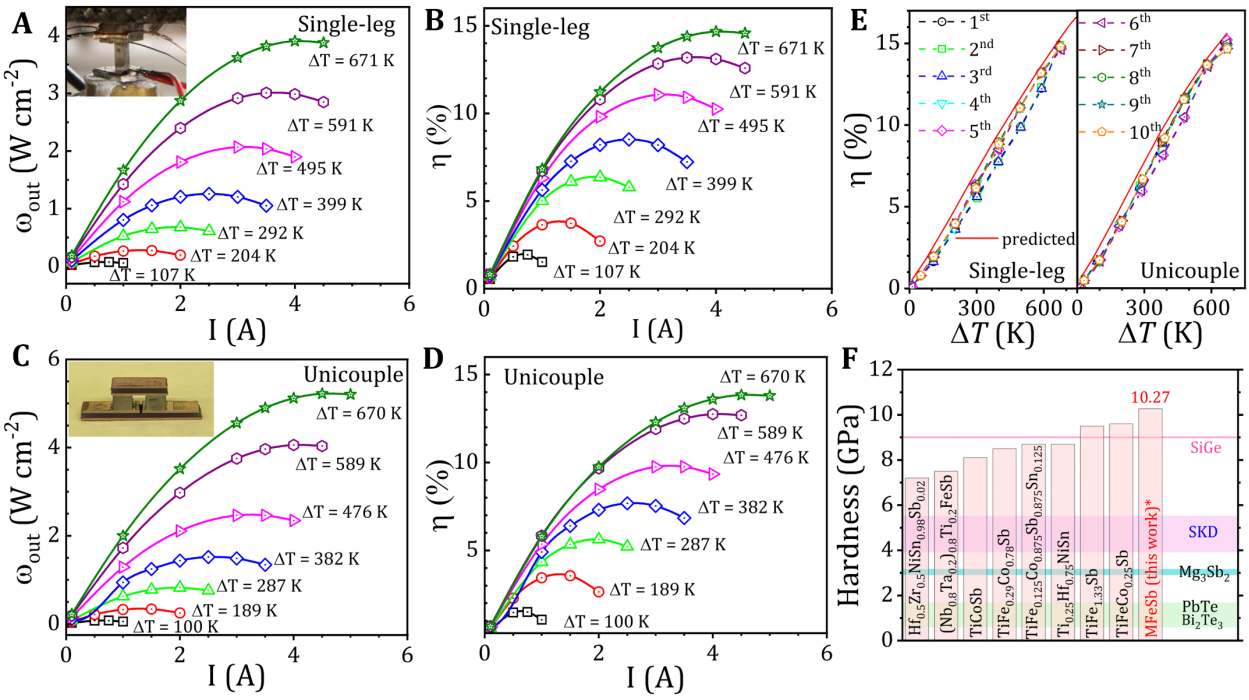

Figure 5. TE device performance and mechanical properties.
(A and B) Single-leg device performance. The current dependence of (A) output leg power density (ω_{out}) and (B) η.
(C and D) Unicouple module performance. The current dependence of (C) ω_{out} and (D) η.
(E) The η as a function of ΔT for multiple tests. The calculated theoretical efficiency for both single-leg and unicouple devices are denoted with a solid line (Red).
(F) Comparison of mechanical hardness in MFeSb with other state-of-the-art TE materials.[3,22,59,60]

CONCLUSION

In conclusion, we have successfully demonstrated the formation of single-phase high-entropy hH thermoelectric material by enhancing S_{conf} with competitive TE performance. High-entropy engineering has proven effective in preserving superior electrical transport properties through entropy-driven structural stabilization. Simultaneously, the introduction of chemical complexity in the high-entropy material induces substantial lattice strains within a short-range order, resulting in a distorted lattice. This phenomenon significantly enhances the scattering of heat-carrying

phonons, leading to remarkably low lattice thermal conductivity. As a result, our designed high-entropy hH alloy attained a superior zT ~1.5 at 1060 K, making the highest zT_{avg} of 0.92 within the temperature range of 300-1060 K. Furthermore, the exceptional η reached to 15% and 14% for single-leg and unicouple module at ΔT of 672 K, respectively. Additionally, these alloys also demonstrate high mechanical performance (hardness of 10.3 GPa) making them ideal for practical applications where high structural compatibility is demanding. Our study suggests that the design of high-entropy material, achieved by enhancing S_{conf}, can effectively improve TE performance by simultaneously optimizing electrical and thermal transport.

ACKNOWLEDGEMENTS

This work is primarily supported via the US ARMY RIF program. S.G., and W.L. acknowledge the financial support from the Army RIF program (contract number W911W6-19-C-0083). A.N. acknowledges the support through the Office of Naval Research (ONR) through award number N00014-20-1-2602. Y. X. acknowledges the support from the US National Science Foundation through award 2317008. H. L. was supported by the MOTIE (Ministry of Trade, Industry, and Energy) in Korea, under the Fostering Global Talents for Innovative Growth Program (P0008750) supervised by the Korea Institute for Advancement of Technology (KIAT). B.P. acknowledge the financial support from the NSF IUCRC program through CEHMS.

AUTHOR CONTRIBUTION

S.G. and W.L. conceived and designed the experiments. S.G. synthesized the samples and carried out thermoelectric analysis. Y.X. and H.L. performed theoretical analysis. S.G. and W.L. performed the device performance. L.R. carried out EBSD characterization. S.S. performed the metallization of the sample. S.K.K. measured sound velocity. J.G. performed the TEM characterization. S.G., W.L., and A.N. worked on the visualization and validation of the results. S.G. and Y.X. prepared the initial draft of the manuscript. B.P. and W.L. supervised the project. All the authors discussed the research data, reviewed, and edited the writing.

DECLERATAION OF INTERESTS

The authors declare no competing interests.

SUPPLEMENTAL INFORMATION

Figures S1–S25 and

Table S1-S3

REFERENCES

1. Bell, L.E. (2008). Cooling, Heating, Generating Power, and Recovering Waste Heat with Thermoelectric Systems. Science *321*, 1457–1461. 10.1126/science.1158899.

2. Poudel, B., Hao, Q., Ma, Y., Lan, Y., Minnich, A., Yu, B., Yan, X., Wang, D., Muto, A., Vashaee, D., et al. (2008). High-Thermoelectric Performance of Nanostructured Bismuth Antimony Telluride Bulk Alloys. Science *320*, 634–638. 10.1126/science.1156446.

3. Yan, Q., and Kanatzidis, M.G. (2022). High-performance thermoelectrics and challenges for practical devices. Nat. Mater. *21*, 503–513. 10.1038/s41563-021-01109-w.

4. Xing, Y., Liu, R., Liao, J., Wang, C., Zhang, Q., Song, Q., Xia, X., Zhu, T., Bai, S., and Chen, L. (2020). A Device-to-Material Strategy Guiding the "Double-High" Thermoelectric Module. Joule *4*, 2475–2483. 10.1016/j.joule.2020.08.009.

5. Li, W., Ghosh, S., Liu, N., and Poudel, B. (2024). Half-Heusler thermoelectrics: Advances from materials fundamental to device engineering. Joule *8*, 1274–1311. 10.1016/j.joule.2024.03.016.

6. Zeier, W.G., Schmitt, J., Hautier, G., Aydemir, U., Gibbs, Z.M., Felser, C., and Snyder, G.J. (2016). Engineering half-Heusler thermoelectric materials using Zintl chemistry. Nat. Rev. Mater. *1*, 16032. 10.1038/natrevmats.2016.32.

7. Zhou, C., Lee, Y.K., Yu, Y., Byun, S., Luo, Z.-Z., Lee, H., Ge, B., Lee, Y.-L., Chen, X., Lee, J.Y., et al. (2021). Polycrystalline SnSe with a thermoelectric figure of merit greater than the single crystal. Nat. Mater. *20*, 1378–1384. 10.1038/s41563-021-01064-6.

8. Jiang, B., Wang, W., Liu, S., Wang, Y., Wang, C., Chen, Y., Xie, L., Huang, M., and He, J. (2022). High figure-of-merit and power generation in high-entropy GeTe-based thermoelectrics. Science *377*, 208–213. 10.1126/science.abq5815.

9. Jiang, B., Yu, Y., Cui, J., Liu, X., Xie, L., Liao, J., Zhang, Q., Huang, Y., Ning, S., Jia, B., et al. (2021). High-entropy-stabilized chalcogenides with high thermoelectric performance. Science *371*, 830–834. 10.1126/science.abe1292.

10. Fu, C., Zhu, T., Pei, Y., Xie, H., Wang, H., Snyder, G.J., Liu, Y., Liu, Y., and Zhao, X. (2014). High Band Degeneracy Contributes to High Thermoelectric Performance in p-Type Half-Heusler Compounds. Adv. Energy Mater. *4*, 1400600. 10.1002/aenm.201400600.

11. Mao, J., Chen, G., and Ren, Z. (2021). Thermoelectric cooling materials. Nat. Mater. *20*, 454–461. 10.1038/s41563-020-00852-w.

12. Roychowdhury, S., Ghosh, T., Arora, R., Samanta, M., Xie, L., Singh, N.K., Soni, A., He, J., Waghmare, U. V., and Biswas, K. (2021). Enhanced atomic ordering leads to high thermoelectric performance in AgSbTe 2. Science *371*, 722–727. 10.1126/science.abb3517.

13. Pei, Y., Wang, H., and Snyder, G.J. (2012). Band Engineering of Thermoelectric Materials. Adv. Mater. *24*, 6125–6135. 10.1002/adma.201202919.

14. Fu, C., Zhu, T., Liu, Y., Xie, H., and Zhao, X. (2015). Band engineering of high performance p-type FeNbSb based half-Heusler thermoelectric materials for figure of merit zT > 1. Energy Environ. Sci. *8*, 216–220. 10.1039/C4EE03042G.

15. Sahu, A., Russ, B., Liu, M., Yang, F., Zaia, E.W., Gordon, M.P., Forster, J.D., Zhang, Y.-Q., Scott, M.C., Persson, K.A., et al. (2020). In-situ resonant band engineering of solution-processed semiconductors generates high performance n-type thermoelectric nano-inks. Nat. Commun. *11*, 2069. 10.1038/s41467-020-15933-2.

16. Mori, T. (2017). Novel Principles and Nanostructuring Methods for Enhanced Thermoelectrics. Small *13*, 1702013. 10.1002/smll.201702013.

17. Jiang, B., Yu, Y., Chen, H., Cui, J., Liu, X., Xie, L., and He, J. (2021). Entropy engineering promotes thermoelectric performance in p-type chalcogenides. Nat. Commun. *12*, 3234. 10.1038/s41467-021-23569-z.

18. Korkosz, R.J., Chasapis, T.C., Lo, S., Doak, J.W., Kim, Y.J., Wu, C., Hatzikraniotis, E., Hogan, T.P., Seidman, D.N., Wolverton, C., et al. (2014). High ZT in p-Type (PbTe) 1–2 x (PbSe) x (PbS) x Thermoelectric Materials. J. Am. Chem. Soc. *136*, 3225–3237. 10.1021/ja4121583.

19. George, E.P., Raabe, D., and Ritchie, R.O. (2019). High-entropy alloys. Nat. Rev. Mater. *4*, 515–534. 10.1038/s41578-019-0121-4.

20. Wang, H., He, Q., Gao, X., Shang, Y., Zhu, W., Zhao, W., Chen, Z., Gong, H., and Yang, Y. (2023). Multifunctional High Entropy Alloy Enabled by Severe Lattice Distortion. Adv. Mater., doi: 10.1002/adma.202305453. 10.1002/adma.202305453.

21. Zhu, H., Li, W., Nozariasbmarz, A., Liu, N., Zhang, Y., Priya, S., and Poudel, B. (2023). Half-Heusler alloys as emerging high power density thermoelectric cooling materials. Nat. Commun. *14*, 3300. 10.1038/s41467-023-38446-0.

22. Rogl, G., Grytsiv, A., Gürth, M., Tavassoli, A., Ebner, C., Wünschek, A., Puchegger, S., Soprunyuk, V., Schranz, W., Bauer, E., et al. (2016). Mechanical properties of half-Heusler alloys. Acta Mater. *107*, 178–195. 10.1016/j.actamat.2016.01.031.

23. Fu, C., Bai, S., Liu, Y., Tang, Y., Chen, L., Zhao, X., and Zhu, T. (2015). Realizing high figure of merit in heavy-band p-type half-Heusler thermoelectric materials. Nat. Commun. *6*, 8144. 10.1038/ncomms9144.

24. Zhu, H., He, R., Mao, J., Zhu, Q., Li, C., Sun, J., Ren, W., Wang, Y., Liu, Z., Tang, Z., et al. (2018). Discovery of ZrCoBi based half Heuslers with high thermoelectric conversion efficiency. Nat. Commun. *9*, 2497. 10.1038/s41467-018-04958-3.

25. Yan, X., Liu, W., Wang, H., Chen, S., Shiomi, J., Esfarjani, K., Wang, H., Wang, D., Chen, G., and Ren, Z. (2012). Stronger phonon scattering by larger differences in atomic mass and size in p-type half-Heuslers Hf1−xTixCoSb0.8Sn0.2. Energy Environ. Sci. *5*, 7543. 10.1039/c2ee21554c.

26. Zhu, H., Mao, J., Li, Y., Sun, J., Wang, Y., Zhu, Q., Li, G., Song, Q., Zhou, J., Fu, Y., et al. (2019). Discovery of TaFeSb-based half-Heuslers with high thermoelectric performance. Nat. Commun. *10*, 270. 10.1038/s41467-018-08223-5.

27. Simonson, J.W., Wu, D., Xie, W.J., Tritt, T.M., and Poon, S.J. (2011). Introduction of resonant states and enhancement of thermoelectric properties in half-Heusler alloys. Phys. Rev. B *83*, 235211. 10.1103/PhysRevB.83.235211.

28. Chen, K., Zhang, R., Bos, J.-W.G., and Reece, M.J. (2022). Synthesis and thermoelectric properties of high-entropy half-Heusler MFe1−xCoxSb (M = equimolar Ti, Zr, Hf, V, Nb, Ta). J. Alloys Compd. *892*, 162045. 10.1016/j.jallcom.2021.162045.

29. He, R., Kraemer, D., Mao, J., Zeng, L., Jie, Q., Lan, Y., Li, C., Shuai, J., Kim, H.S., Liu, Y., et al. (2016). Achieving high power factor and output power density in p-type half-Heuslers Nb 1-x Ti x FeSb. Proc. Natl. Acad. Sci. *113*, 13576–13581. 10.1073/pnas.1617663113.

30. Yan, J., Liu, F., Ma, G., Gong, B., Zhu, J., Wang, X., Ao, W., Zhang, C., Li, Y., and Li, J. (2018). Suppression of the lattice thermal conductivity in NbFeSb-based half-Heusler thermoelectric materials through high entropy effects. Scr. Mater. *157*, 129–134. 10.1016/j.scriptamat.2018.08.008.

31. Kang, H.B., Poudel, B., Li, W., Lee, H., Saparamadu, U., Nozariasbmarz, A., Kang, M.G., Gupta, A., Heremans, J.J., and Priya, S. (2020). Decoupled phononic-electronic transport in multi-phase n-type half-Heusler nanocomposites enabling efficient high temperature power generation. Mater. Today *36*, 63–72. 10.1016/j.mattod.2020.01.002.

32. Xing, Y., Liu, R., Liao, J., Zhang, Q., Xia, X., Wang, C., Huang, H., Chu, J., Gu, M., Zhu, T., et al. (2019). High-efficiency half-Heusler thermoelectric modules enabled by self-propagating synthesis and topologic structure optimization. Energy Environ. Sci. *12*, 3390–3399. 10.1039/C9EE02228G.

33. Qiu, P., Mao, T., Huang, Z., Xia, X., Liao, J., Agne, M.T., Gu, M., Zhang, Q., Ren, D., Bai, S., et al. (2019). High-Efficiency and Stable Thermoelectric Module Based on Liquid-Like Materials. Joule *3*, 1538–1548. 10.1016/j.joule.2019.04.010.

34. Nie, G., Li, W., Guo, J., Yamamoto, A., Kimura, K., Zhang, X., Isaacs, E.B., Dravid, V., Wolverton, C., Kanatzidis, M.G., et al. (2019). High performance thermoelectric module through isotype bulk heterojunction engineering of skutterudite materials. Nano Energy *66*, 104193. 10.1016/j.nanoen.2019.104193.

35. Liu, D., Wang, D., Hong, T., Wang, Z., Wang, Y., Qin, Y., Su, L., Yang, T., Gao, X., Ge, Z., et al. (2023). Lattice plainification advances highly effective SnSe crystalline thermoelectrics. Science *380*, 841–846. 10.1126/science.adg7196.

36. Wu, X., Lin, Y., Han, Z., Li, H., Liu, C., Wang, Y., Zhang, P., Zhu, K., Jiang, F., Huang, J., et al. (2022). Interface and Surface Engineering Realized High Efficiency of 13% and Improved Thermal Stability in Mg 3 Sb 1.5 Bi 0.5 -Based Thermoelectric Generation Devices. Adv. Energy Mater. *12*, 2203039. 10.1002/aenm.202203039.

37. Zhang, Q., Zhou, Z., Dylla, M., Agne, M.T., Pei, Y., Wang, L., Tang, Y., Liao, J., Li, J., Bai, S., et al. (2017). Realizing high-performance thermoelectric power generation through grain boundary engineering of skutterudite-based nanocomposites. Nano Energy *41*, 501–510. 10.1016/j.nanoen.2017.10.003.

38. Xie, L., Ming, C., Song, Q., Wang, C., Liao, J., Wang, L., Zhu, C., Xu, F., Sun, Y.Y., Bai, S., et al. (2023). Lead-free and scalable GeTe-based thermoelectric module with an efficiency of 12. Sci. Adv. *9*, eadg7919. 10.1126/sciadv.adg7919.

39. Jia, B., Huang, Y., Wang, Y., Zhou, Y., Zhao, X., Ning, S., Xu, X., Lin, P., Chen, Z., Jiang, B., et al. (2022). Realizing high thermoelectric performance in non-nanostructured n-type PbTe. Energy Environ. Sci. *15*, 1920–1929. 10.1039/D1EE03883D.

40. Zhang, Y., Li, Z., Singh, S., Nozariasbmarz, A., Li, W., Genç, A., Xia, Y., Zheng, L., Lee, S.H., Karan, S.K., et al. (2023). Defect-Engineering-Stabilized AgSbTe 2 with High Thermoelectric Performance. Adv. Mater. *35*, 2208994. 10.1002/adma.202208994.

41. Li, W., Poudel, B., Kishore, R.A., Nozariasbmarz, A., Liu, N., Zhang, Y., and Priya, S. (2023). Toward High Conversion Efficiency of Thermoelectric Modules through Synergistical Optimization of Layered Materials. Adv. Mater. *35*, 2210407. 10.1002/adma.202210407.

42. Yang, J., Meisner, G.P., and Chen, L. (2004). Strain field fluctuation effects on lattice thermal conductivity of ZrNiSn-based thermoelectric compounds. Appl. Phys. Lett. *85*, 1140–1142. 10.1063/1.1783022.

43. Yu, J., Fu, C., Liu, Y., Xia, K., Aydemir, U., Chasapis, T.C., Snyder, G.J., Zhao, X., and Zhu, T. (2018). Unique Role of Refractory Ta Alloying in Enhancing the Figure of Merit of NbFeSb Thermoelectric Materials. Adv. Energy Mater. *8*, 1701313. 10.1002/aenm.201701313.

44. Xie, H., Wang, H., Fu, C., Liu, Y., Snyder, G.J., Zhao, X., and Zhu, T. (2014). The intrinsic disorder related alloy scattering in ZrNiSn half-Heusler thermoelectric materials. Sci. Rep. *4*, 6888. 10.1038/srep06888.

45. Fang, T., Zheng, S., Chen, H., Cheng, H., Wang, L., and Zhang, P. (2016). Electronic structure and thermoelectric properties of p-type half-Heusler compound NbFeSb: a first-principles study. RSC Adv. *6*, 10507–10512. 10.1039/C5RA23091H.

46. Zunger, A., Wei, S.-H., Ferreira, L.G., and Bernard, J.E. (1990). Special quasirandom structures. Phys. Rev. Lett. *65*, 353–356. 10.1103/PhysRevLett.65.353.

47. Popescu, V., and Zunger, A. (2012). Extracting E versus k effective band structure from supercell calculations on alloys and impurities. Phys. Rev. B *85*, 085201. 10.1103/PhysRevB.85.085201.

48. Han, S., Dai, S., Ma, J., Ren, Q., Hu, C., Gao, Z., Duc Le, M., Sheptyakov, D., Miao, P., Torii, S., et al. (2023). Strong phonon softening and avoided crossing in aliovalence-doped heavy-band thermoelectrics. Nat. Phys. *19*, 1649–1657. 10.1038/s41567-023-02188-z.

49. Wallace, D.C. (1998). Thermodynamics of Crystals, Dover Books on Physics (Dover).

50. Novikov, I.S., Gubaev, K., Podryabinkin, E. V, and Shapeev, A. V (2021). The MLIP package: moment tensor potentials with MPI and active learning. Mach. Learn. Sci. Technol. *2*, 025002. 10.1088/2632-2153/abc9fe.

51. Gubaev, K., Podryabinkin, E. V., Hart, G.L.W., and Shapeev, A. V. (2019). Accelerating high-throughput

searches for new alloys with active learning of interatomic potentials. Comput. Mater. Sci. *156*, 148–156. 10.1016/j.commatsci.2018.09.031.

52. Zhang, H., Xiong, S., Wang, H., Volz, S., and Ni, Y. (2019). Thermal transport in graphene/h-BN lateral heterostructures with interface compositional diffusion. EPL (Europhysics Lett. *125*, 46001. 10.1209/0295-5075/125/46001.

53. Biswas, R., Bouchard, A.M., Kamitakahara, W.A., Grest, G.S., and Soukoulis, C.M. (1988). Vibrational Localization in Amorphous Silicon. Phys. Rev. Lett. *60*, 2280–2283. 10.1103/PhysRevLett.60.2280.

54. Loh, G.C., Teo, E.H.T., and Tay, B.K. (2012). Phonon localization around vacancies in graphene nanoribbons. Diam. Relat. Mater. *23*, 88–92. 10.1016/j.diamond.2012.01.006.

55. Joshi, G., Dahal, T., Chen, S., Wang, H., Shiomi, J., Chen, G., and Ren, Z. (2013). Enhancement of thermoelectric figure-of-merit at low temperatures by titanium substitution for hafnium in n-type half-Heuslers Hf0.75−Ti Zr0.25NiSn0.99Sb0.01. Nano Energy *2*, 82–87. 10.1016/j.nanoen.2012.07.020.

56. Li, W., Poudel, B., Nozariasbmarz, A., Sriramdas, R., Zhu, H., Kang, H.B., and Priya, S. (2020). Bismuth Telluride/Half-Heusler Segmented Thermoelectric Unicouple Modules Provide 12% Conversion Efficiency. Adv. Energy Mater. *10*, 2001924. 10.1002/aenm.202001924.

57. Wei, S., Kim, S.J., Kang, J., Zhang, Y., Zhang, Y., Furuhara, T., Park, E.S., and Tasan, C.C. (2020). Natural-mixing guided design of refractory high-entropy alloys with as-cast tensile ductility. Nat. Mater. *19*, 1175–1181. 10.1038/s41563-020-0750-4.

58. Li, T., Liu, T., Zhao, S., Chen, Y., Luan, J., Jiao, Z., Ritchie, R.O., and Dai, L. (2023). Ultra-strong tungsten refractory high-entropy alloy via stepwise controllable coherent nanoprecipitations. Nat. Commun. *14*, 3006. 10.1038/s41467-023-38531-4.

59. Yu, J., Xing, Y., Hu, C., Huang, Z., Qiu, Q., Wang, C., Xia, K., Wang, Z., Bai, S., Zhao, X., et al. (2020). Half-Heusler Thermoelectric Module with High Conversion Efficiency and High Power Density. Adv. Energy Mater. *10*, 2000888. 10.1002/aenm.202000888.

60. Bathula, S., Jayasimhadri, M., and Dhar, A. (2015). Mechanical properties and microstructure of spark plasma sintered nanostructured p-type SiGe thermoelectric alloys. Mater. Des. *87*, 414–420. 10.1016/j.matdes.2015.08.017.